Nanoscale Advances

ROYAL SOCIETY OF CHEMISTRY

PAPER

View Article Online
View Journal



Cite this: DOI: 10.1039/d5na01186h

# Chemical vapor deposition growth and characterization of $ReSe_2$

J. Onasanya,*[a] Mourad Benamara,[b] Kanagaraj Moorthi,[b] H. O. H. Churchill,[abc] Bothina Hamad *[ac] and M. O. Manasreh[d]

Received 30th December 2025
Accepted 12th March 2026

DOI: 10.1039/d5na01186h

rsc.li/nanoscale-advances

Two-dimensional (2D) $ReSe_2$ flakes were grown by chemical vapor deposition and investigated at room temperature using Raman, photoluminescence, and absorption spectroscopies. The Raman spectra revealed eighteen phonon modes in the range of 100–300 $cm^{-1}$, which were found to be in good agreement with the density functional theory (DFT) calculations. The thickness profiles of the $ReSe_2$ flakes are in the range of 5–50 nm. The $ReSe_2$ crystal structure and morphology were investigated using XRD, atomic force microscopy and scanning electron microscopy. Energy dispersion spectroscopy confirmed the 1 : 2 elemental composition. The absorption spectra of $ReSe_2$ flakes exhibited excitonic peaks in the spectral region of 885–942 nm (1.401–1.316 eV). These peaks are used to define the band gap of the material. The DFT calculations predicted an indirect bandgap of 0.88 eV for the bulk structure, while a direct bandgap of 1.26 eV was predicted for the monolayer.



## 1. Introduction

Two-dimensional (2D) chalcogenide materials have attracted considerable interest due to their strong in-plane covalent bonds, which contrast with the weak van der Waals interlayer bonds. These van der Waals interactions allow easy mechanical exfoliation at the atomic level, where electron confinement plays a major role.[1–3] This crystallographic nature leads to intriguing electrical and optoelectronic device characteristics, such as carrier mobility, exciton binding energy, phonon scattering, and thermal conductivity.[4–10] Among these 2D materials, there is an emerging class of low-symmetry materials with orthorhombic, monoclinic, or triclinic crystal structures with unique in-plane lattice arrangements that lead to in-plane orientation-dependent physical properties.[11–14] The distinct characteristics of these materials result in anisotropic electronic and optical properties that are promising for applications in polarization-based optical devices.[15,16] Black phosphorus (BP) is the first known low-symmetry 2D semiconductor layered material with a puckered honeycomb arrangement. It possesses strong in-plane optical anisotropy due to its orthorhombic crystal structure. Like other well-known 2D layered materials, it exhibits excellent properties for potential application in optoelectronics.[17] However, there are limitations to the broader use of BP due to its poor environmental stability leading to degradation due to oxidation under ambient conditions.[18] Therefore, there is a challenge in synthesizing high-quality and large-area flakes.[19] These highlighted limitations of BP have inspired research into alternative low-symmetry materials with environmental stability such as rhenium dichalcogenides, $ReX_2$ (X = S, Se). Rhenium dichalcogenides fall into the class of transition metal dichalcogenides that crystallize in a distorted triclinic structure with a $\bar{P}1$ space group.[20] This structure adopts a distorted $CdCl_2$ type configuration,[21,22] arising from the Re–Re zigzag chains formed within each layer, which breaks the in-plane symmetry. These properties lead to anisotropic optical and electronic properties, tunable bandgaps, and pronounced nonlinear optical responses,[23,24] making them ideal for applications in ultrafast photonics and high-performance photodetectors, while enabling new applications in polarization-sensitive technologies.[25,26]

Several methods have been reported for the synthesis of $ReX_2$ (X = S, Se), such as mechanical exfoliation, chemical vapor transport, liquid phase exfoliation, hydrothermal synthesis, and chemical vapor deposition (CVD).[27] Among these methods, the CVD technique offers precise control over material growth parameters, which is an essential feature for producing high-quality 2D materials such as rhenium diselenide ($ReSe_2$).[28] Li *et al.* reported the CVD growth of high quality vertically aligned $ReSe_2$ nanosheets directly on conductive substrates, resulting in effective growth at temperatures near 450 °C[25,29]

In this article, we report the structural, electronic, and optical properties of high purity $ReSe_2$ flakes synthesized by the CVD technique. The morphology and elemental composition were analyzed using scanning electron microscopy (SEM),

[a]Materials Science and Engineering, University of Arkansas, Fayetteville, AR 72701, USA. E-mail: onasanya@uark.edu; bothinah@uark.edu

[b]Institute for Nanoscale Science and Engineering, University of Arkansas, Fayetteville, AR 72701, USA

[c]Department of Physics, University of Arkansas, Fayetteville, AR 72701, USA

[d]Department of Electrical Engineering and Computer Science, University of Arkansas, Fayetteville, AR 72701, USA

atomic force microscopy (AFM) and energy dispersive spectroscopy (EDS). The obtained images of the synthesized flakes show a triclinic crystal symmetry. The experimentally observed Raman spectra, using μ-Raman spectroscopy, revealed 18 phonon modes that are in good agreement with the DFT calculated results. Optical absorption measurements showed distinct excitonic peaks, and X-ray diffraction (XRD) analysis confirmed the quality of the $ReSe_2$ crystals with sharp diffraction peaks. The successful growth of $ReSe_2$ flakes is encouraging toward the fabrication of optoelectronic devices.

## 2. Theory and experiment

This section presents the theoretical and experimental investigations of 2D $ReSe_2$ flakes grown by a CVD method. The theoretical calculations were performed using the DFT approach as implemented in the Vienna *ab initio* simulation package (VASP).[30,31] The generalized gradient approximation (GGA) with the Perdew–Burke–Ernzerhof (PBE) functional was adopted for the exchange-correlation treatment.[32] The van der Waals interactions were considered in these calculations using the optB86b functional.[33] A plane-wave cutoff energy of 550 eV was employed with the energy convergence criterion set at $10^{-8}$ eV. The Brillouin zone was sampled using $9 \times 9 \times 8$ and $9 \times 9 \times 1$ Monkhorst–Pack *K*-point grids for the bulk and monolayer systems, respectively. The density functional perturbation theory (DFPT) technique[34] was used to obtain the phonon modes at the gamma point. The layered stacking of bulk $ReSe_2$ exhibits a distorted triclinic phase, known as Peierls distortion. In this phase, rhenium atoms are sandwiched between the selenium atoms, see Fig. 1(a), where the Re atoms form Re–Re chains with a diamond shape, as indicated by the red line in Fig. 1(b).

Rhenium diselenide single crystal flakes with various thicknesses were synthesized using a CVD growth method. As precursors, 100 mg of ammonium perrhenate ($NH_4ReO_4$, 99.9% purity) and 500 mg of selenium powdered were used. These materials were purchased from Strem Chemicals, Inc. A mixed gas of argon and hydrogen in a ratio of 4 : 1 was used as the carrier for the mass transport of thermally evaporated chemical species inside the growth quartz tube with a flow rate of 30 sccm. The growth process was conducted in a horizontal tube furnace at a temperature of 700 °C. The furnace was initially purged with Ar gas to remove any residual oxygen, ensuring an inert atmosphere. The growth time was maintained for 30 minutes to facilitate the formation of $ReSe_2$ flakes.

A Horiba LabRAM HR spectrometer was used to obtain the μ-photoluminescence (PL) and μ-Raman spectra. A HeNe laser with a wavelength of 632.8 nm was used to excite the Raman vibrational modes in the spectral range of 100–300 $cm^{-1}$. A cobalt laser with a wavelength of 472.9 nm was used for PL measurements over the spectral range of 450–1100 nm. Angle-resolved polarized Raman spectroscopy was carried out to determine the in-plane anisotropy and crystallographic orientation of the sample. Polarization rotation was achieved by rotating a half-wave plate through angles ranging from 0° to 360° in 10° increments. At each angle, Raman spectra were collected under identical integration conditions and processed to extract peak intensities. The absorbance spectrum was obtained using a Cary 500 UV-Visible-NIR spectrometer (Agilent Technologies). The structural analysis of the synthesized $ReSe_2$ was conducted using an X-ray diffractometer (Rigaku Miniflex) equipped with Cu Kα radiation ($\lambda$ = 1.5406 Å). Diffraction patterns over a $2\theta$ range of 10°–60° were collected to identify the crystalline phases and assess the quality of the deposited layers. A Bruker D3100 Nanoscope AFM, equipped with a tapping mode module, was utilized to investigate the surface morphology of the grown flakes. The scanning electron microscopy (SEM) images were obtained by using a FEI Nova Nanolab 200 fitted with a Bruker EDS detector.

## 3. Results and discussion

The AFM characterization of $ReSe_2$ flakes grown on a $SiO_2$/Si substrate is shown in Fig. 2(a), with a height distribution ranging from 5 to 50 nm, as indicated by the profile height scan. The surface topography as presented in Fig. 2(b) reveals the flake morphology with varying thickness across the scanned area. The line profile corresponds to the flake thickness, with the green, blue, and red markers indicating values of 50, 10, and 5 nm, respectively. It is observed that the bright island spots are

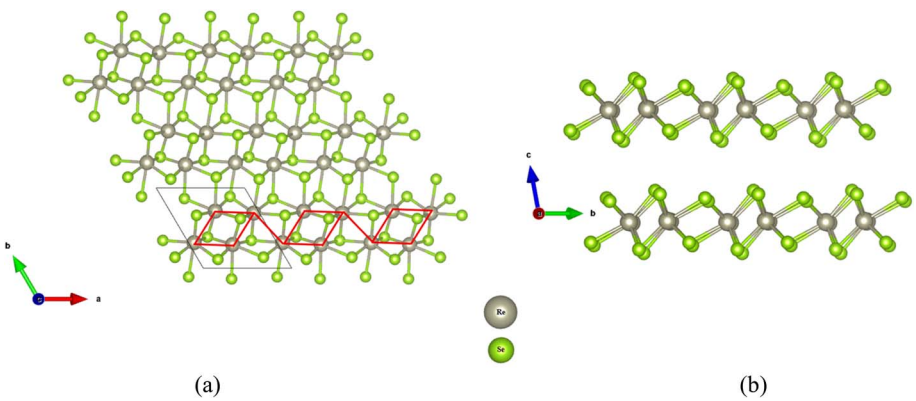


Fig. 1 (a)Side view of the bulk $ReSe_2$ structure with Re atoms sandwiched between Se atoms. (b) Top view showing the zig-zig arrangement of Re atoms as indicated by the red line. Grey and green colors indicate Re and Se atoms, respectively.

 

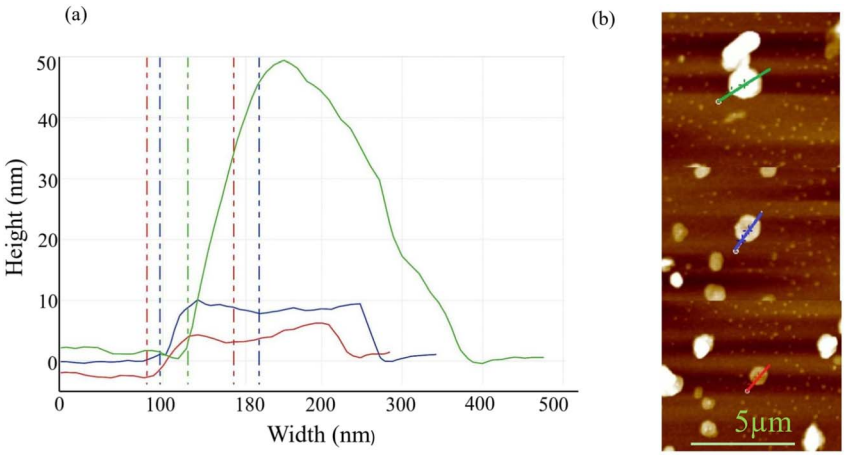


Fig. 2 (a) Height profile measurement of scanned flakes, the colors correspond to each identified spot on the AFM image. (b) AFM image showing the grown $ReSe_2$ flakes.

thicker in dimensions than the dim ones. Therefore, the variation in height is suggestive of multilayered $ReSe_2$ formation ranging from few to several layers in agreement with Hafeez *et al.*[35] The surface morphology of $ReSe_2$ flakes is obtained by SEM as shown in Fig. 3. The SEM images exhibit different shapes and sizes in the grown sample, including hexagonal-like and flower-like shapes. A high-magnification image of 120 00× is shown in Fig. 3(b), corresponding to the lower left region of Fig. 3(a). It reveals the formation of vertical nanosheets stacked in different positions to form dense nanoflowers. The presence of nanosheet clusters and isolated hexagonal structures indicated non-uniformity in the growth process. This behavior has been reported for similarly CVD grown $ReS_2$ flakes, which were described as exhibiting highly dendritic edges.[36] The presence of layered structures as seen from the SEM image is typical for van der Waals 2D layered materials along the basal plane direction.[37] The stoichiometry of the atomic percentage of Re : Se is 1 : 2, as confirmed by the EDS elemental composition reported in Table 1.

The X-ray diffraction (XRD) spectrum shown in Fig. 4 has well-defined peaks at diffraction angles 14.4°, 28.5°, 42.9° and 58.2°, which are readily indexed to the (002), (004), (006), and (008) crystal planes of the layered $ReSe_2$, respectively. These observed peak positions are characteristic of crystalline, layered $ReSe_2$ with distorted triclinic crystal symmetry, which matches the ICDD card no. 04-007-1113.[24,38] We observed no other noticeable peaks except the well resolved XRD patterns of $ReSe_2$, emphasizing the quality of the growth.

The μ-Raman spectra of the grown $ReSe_2$ were taken at room temperature as shown in Fig. 5. This spectrum reveals the presence of the expected and well-defined 18 Raman modes. The experimentally observed Raman modes are consistent with the computational values obtained using the DFPT method,[22,25]

Table 1 Energy-dispersive spectroscopy elemental composition of $ReSe_2$ flakes

| Elements | Series | Concentration (atomic weight %) | Error |
|---|---|---|---|
| Re | L-series | 24.59 | 1.63 |
| Se | L-series | 45.07 | 1.76 |

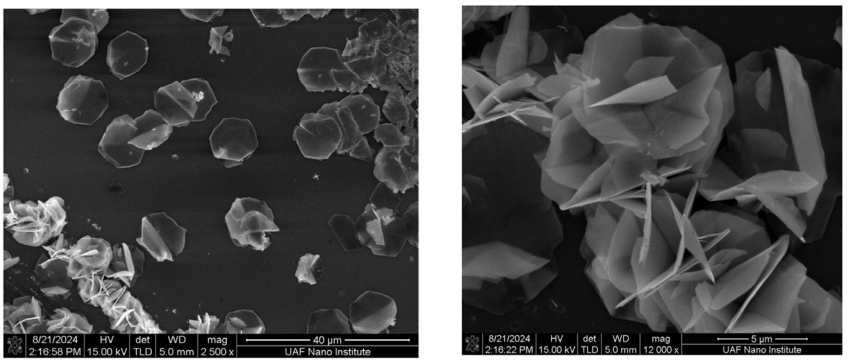


(a) (b)

Fig. 3 (a) SEM image of $ReSe_2$ flakes showing hexagonal- and flower-like layered structures. (b) A high-magnification SEM image of 120 00× that captures the lower left flower-like nanosheets of (a).

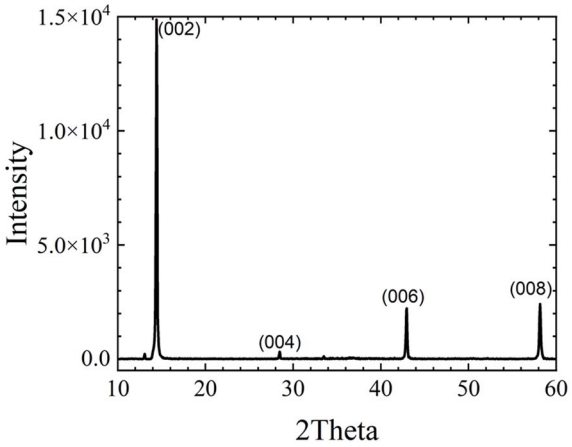


Fig. 4 X-ray diffraction pattern of $ReSe_2$ flakes, showing characteristic peaks at (002), (004), (006), and (008) and preferential orientation along the *c*-axis, typical for 2D layered $ReSe_2$.

as shown in Table 2. These observed Raman modes mostly possess $A_g$ symmetry, which corresponds to in-plane vibrational modes.[39,40] The active Raman modes of vibrations within the short range (100–300 $cm^{-1}$) further indicate the low symmetry properties of $ReSe_2$ with an anisotropic behavior due to its triclinic crystal symmetry. This anisotropic behavior distinguishes its optical and electronics responses[40] from other transition-metal dichalcogenides (TMDs) with high symmetry such as $WS_2$ and $MoS_2$.

The polarization polar plot of three selected Raman modes (125.3, 162, and 177 $cm^{-1}$) from the experimental data was analyzed to understand the optical anisotropy of the grown $ReSe_2$. The resulting polar plot takes the form of a two-lobe shape, characteristic of anisotropic low-symmetric 2D materials.[41] However, the lobes display unequal intensity maxima, indicating a deviation from ideal symmetric anisotropic scattering. This can be attributed to the surface roughness, morphology[42] and thickness variation[43] from the growth

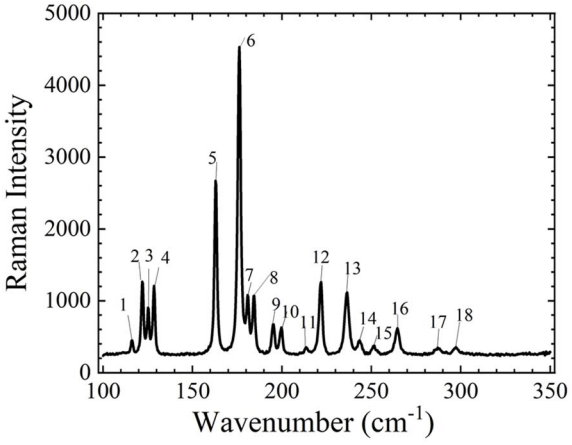


Fig. 5 The micro-Raman spectrum of $ReSe_2$ at room temperature with 18 observable phonon modes in the range of 100–300 $cm^{-1}$. The observed vibrational modes are consistent with the typical triclinic structure of $ReSe_2$ and are in good agreement with DFT calculations.

Table 2 Raman modes of $ReSe_2$, both experimentally measured in Fig. 5 and DFT calculated in the range of 100–300 $cm^{-1}$ with a total of 18 Raman active peaks

| Peak numbers | Experiment ($cm^{-1}$) | Calculated ($cm^{-1}$) | Raman mode |
|---|---|---|---|
| 1 | 116.3 | 112.7 | $A_g$ |
| 2 | 122.1 | 117.9 | $A_g$ |
| 3 | 125.3 | 122.8 | $A_g$ |
| 4 | 128.5 | 125.5 | $A_g$ |
| 5 | 162.3 | 159.4 | $A_g$ |
| 6 | 176.1 | 172.0 | $A_g$ |
| 7 | 180.7 | 177.1 | $A_g$ |
| 8 | 184.2 | 179.9 | $A_g$ |
| 9 | 195.3 | 192.0 | $A_g$ |
| 10 | 200.0 | 195.1 | $A_g$ |
| 11 | 213.6 | 208.2 | $A_g$ |
| 12 | 221.5 | 219.7 | $A_g$ |
| 13 | 236.4 | 236.6 | $A_g$ |
| 14 | 243.5 | 241.3 | $A_g$ |
| 15 | 251.1 | 249.8 | $A_g$ |
| 16 | 264.5 | 262.3 | $A_g$ |
| 17 | 287.5 | 285.1 | $A_g$ |
| 18 | 297.3 | 295.3 | $A_g$ |

process, as evidenced by the SEM image in Fig. 3. This premise resulted in altering the incident polarization and the scattered intensities thereby modifying the effective Raman tensor. To account for the asymmetric behavior and describe the angular dependence of the Raman signal, the scattering intensity is expressed through the Raman tensor ($R$) and the unit polarization vectors of the incident ($e_i$) and scattered ($e_s$) light.[44]

$$I \propto |e_i R e_s|^2 \quad (1)$$

Eqn (2)[11] was used to fit the polar plot, where $\theta$ is the polarization incident angle relative to the crystal, which is oriented along the distorted Re–Re chain where the maximum intensities are observed:

$$I(\theta) \propto v^2 + u^2 \cos^2 C + w^2 \sin^2 \theta + 2v(u + w)\cos\theta \sin\theta \quad (2)$$

where $u$, $v$, and $w$ are the elements for each vibrational mode given by the 2 × 2 matrix $R = \begin{pmatrix} u & v \\ v & w \end{pmatrix}$ and the polarization angle, $\theta$, is obtained from the $\tan 2\theta = \frac{2v}{u - w}$. From the polarization-dependent Raman analysis, the angular dependence of the selected Raman modes (125.3, 162.3, and 177 $cm^{-1}$) was fitted using eqn (2). The results are shown in Fig. 6 where the black squares represent the measured angle-resolved Raman intensities, and the solid red curves correspond to the tensor-based fitted profiles. The vibrational modes at 125.3 and 162.3 $cm^{-1}$ exhibit their maximum intensities near 80° and 260°, whereas the 177 $cm^{-1}$ mode displays a slightly shifted pair of maxima at approximately 75° and 255°. The observed 180° periodicity in the different modes is characteristic of the two-fold angular symmetry expected for strongly anisotropic 2D materials.[45,46] The variation in the polarization angles of maximum intensity among the different modes

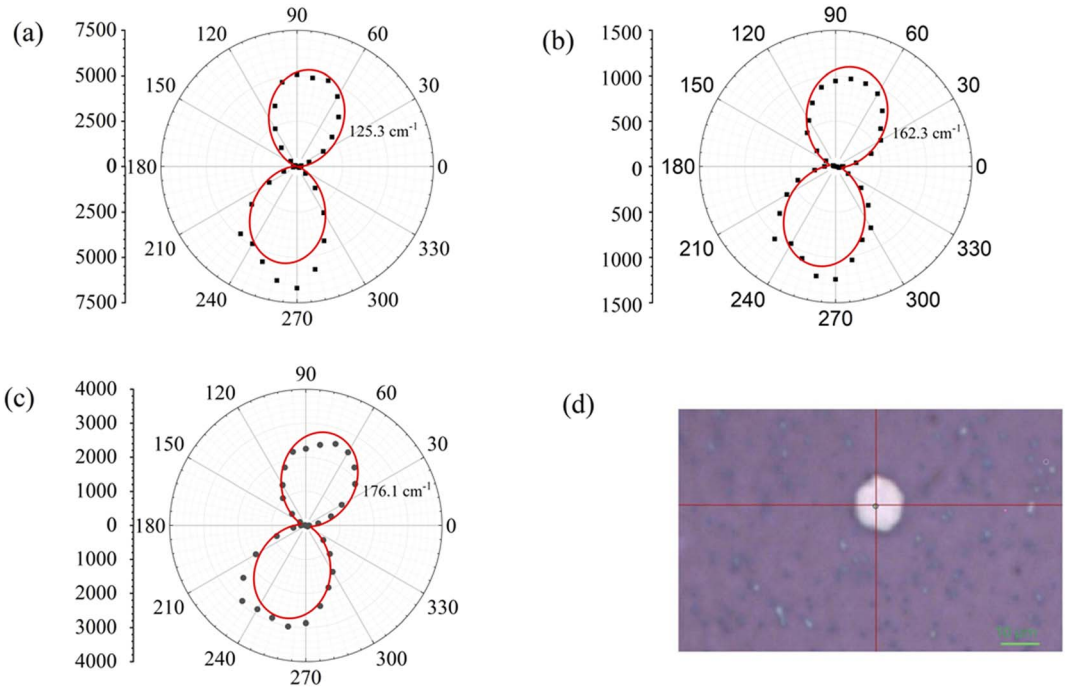


Fig. 6 Angle-resolved polarized Raman polar plots of the vibrational mode intensities at (a) 125.3 (b) 162.3 $cm^{-1}$ and (c) 176.1 $cm^{-1}$ as a function of the polarization angle. Black squares indicate experimental data points, and the solid red line represents the theoretical fit derived from the Raman tensor analysis. (d) Optical microscope image of the scanned $ReSe_2$ flake for polarization measurements.

indicates mode-dependent Raman tensor orientations and reflects the underlying preferential alignment of the distorted Re–Re atomic chains. The results of the fitting tensor parameters and the extracted polarization directions for each mode are summarized in Table 3. The non-zero and non-equivalent values of the tensor fitted parameters ensure the angular dependency for each vibrational mode, this outcome confirms the anisotropic nature of $ReSe_2$.

The Raman mapping spectra of bulk, thick-layer, and few-layers are shown in Fig. 7. The figure shows a noticeable variation in the intensities of the modes, especially the modes located around 125 $cm^{-1}$. However, several peaks show a slight red shift within 1 $cm^{-1}$ as can be clearly observed in the figure inset. This minimal shift agrees with the Raman mapping trends reported by Keyshar *et al.*[36] for $ReS_2$, reflecting the weak interlayer dependence of the distorted 1T′ lattice. The decrease in intensity from bulk to few layer of the vibrational mode might be attributed to thickness dependence or its sensitivity to the Re–Re angular orientation characteristic of the anisotropic $ReSe_2$.[22]

The room-temperature absorption measurement of the grown $ReSe_2$ is presented in Fig. 8. The absorption spectra exhibit two prominent excitonic peaks located at 942 nm (red line) and 885 nm (blue line), corresponding to energy transitions with approximate values of 1.32 eV and 1.40 eV, respectively. These excitonic features indicate a slight layer-dependent variation in the optical bandgap. The obtained bandgap values are consistent with the results reported by Huang *et al.*, who observed temperature-dependent excitonic transitions ranging from 1.36 to 1.42 eV in polarization-resolved absorption measurements between 25 K and 525 K.[47,48] The close agreement between our room-temperature measurements and their temperature-dependent study further validates that excitonic transitions exist regardless of temperature variation. The slight

Table 3 Angle-resolved polarized Raman-tensor fits (*u*, *v*, *w*) and polarization angles ($\theta$)

| Peak ($cm^{-1}$) | *u* | *v* | *w* | $\theta_{max}$ | $\theta_{max}$ + 180° |
|---|---|---|---|---|---|
| 125.3 | 2.40 | 13.02 | 70.95 | 80° | 260° |
| 162.1 | 9.39497 | 5.1785 | 32.25 | 77.8° | 257.8° |
| 176.3 | 15.000 | 10.53908 | 49.99 | 74.5° | 254.5 |

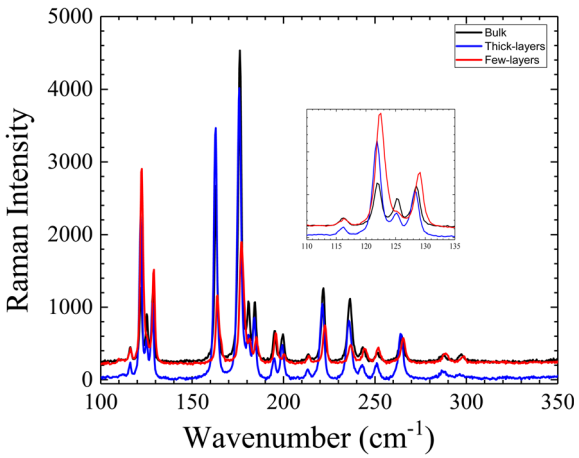


Fig. 7 Raman mapping of bulk, thick-layer, and few-layer $ReSe_2$. Peak positions remain unchanged between bulk and thick layers, while the few-layer region shows a slight red-shift (<1 $cm^{-1}$). The inset highlights the intensity variations of the ~125 $cm^{-1}$ peak thickness.

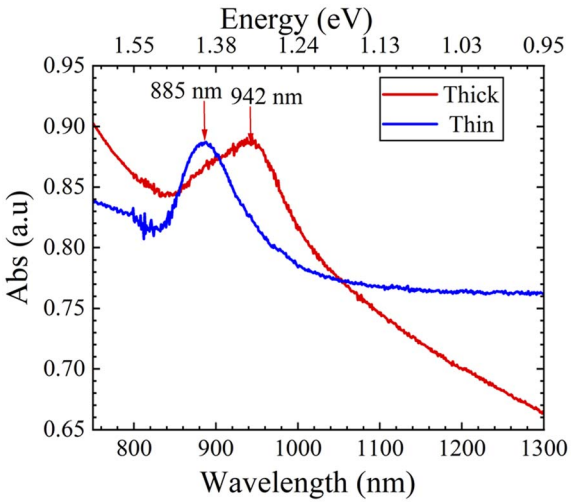


Fig. 8 The room temperature absorbance spectra plot of $ReSe_2$ flakes with observed maximum wavelength peaks at 885 and 942 nm.

blue shift of the higher-energy peak to 1.40 eV in our measurement can be attributed to the reduced layer thickness in the grown flakes. The bandgap showed a slight variation with thickness, suggesting that there is a weak degree of quantum confinement at the nanoscale.[23,49,50] However, it is not pronounced when compared to other traditional TMDs, such as $MoS_2$, $WS_2$, or $ReS_2$ where studies have demonstrated a strong quantum confinement effect.[46,51,52]

The electronic band structure combined with the partial density of states for both bulk and monolayer $ReSe_2$, obtained using DFT calculations, is shown in Fig. 9(a) and (b). The energy bandgap of the bulk is found to be indirect, having an energy value of 0.88 eV[20,22] with the maximum of the valence band located at the $\Gamma$ points, while its conduction band minimum is located between $R$ and $\Gamma$ points. However, the monolayer band structure shows a direct bandgap of 1.26 eV at the $\Gamma$ high symmetry point.[53] Equally, the partial density of states calculation showed the orbital contribution of each element, which perfectly describes the electronic properties in both the bulk and monolayer form. The conduction band is dominated by the d-orbital of the Re atoms while the valence band has almost equal contribution of both the d-orbital of Re and p-orbital of Se atoms. The DFT predicted bandgaps showed a slight observable increase in bandgaps. This further established the weak interlayer dependence of the bandgap as reported in other DFT based studies for $ReSe_2$.[54]

The room temperature PL measurement, represented by the black line in Fig. 10, exhibits a broad spectrum of optical transitions with one main peak around 770 nm (1.60 eV) and two shoulders at 670 nm (1.85 eV) and 860 nm (1.44 eV). This spectrum is fitted with a Gaussian line shape (see a magenta line) to clearly indicate a complex structure with the presence of

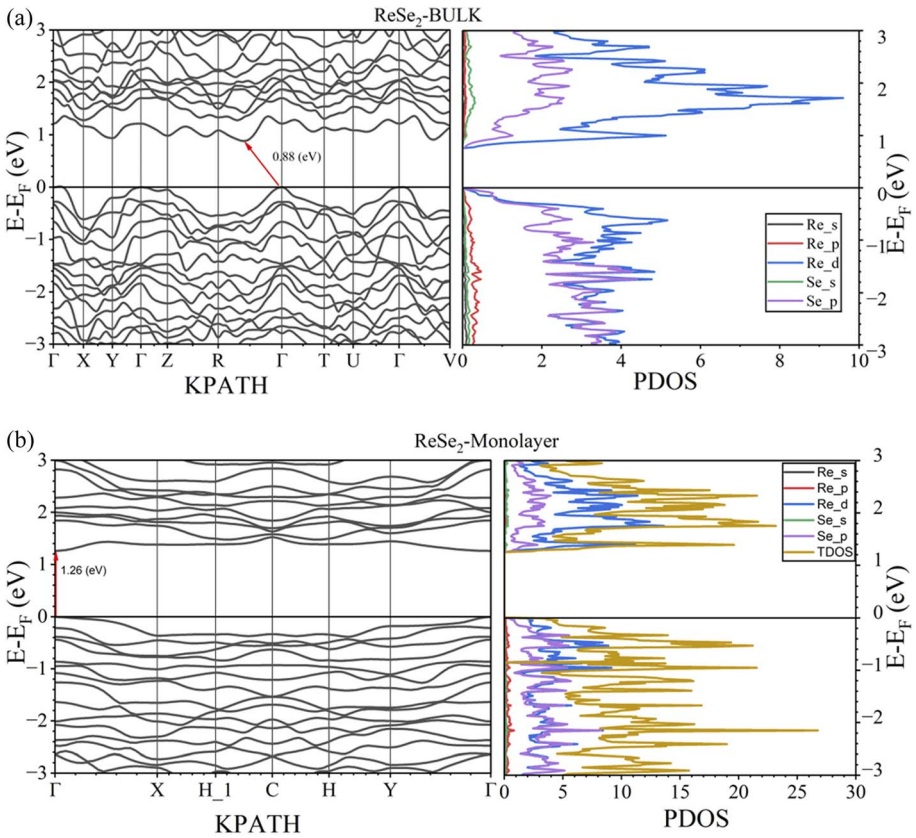


Fig. 9 (a) Density functional theory calculation showing the combined plot of the density of states and energy bandgap for bulk $ReSe_2$ with an energy value of 0.88 eV. (b) Density functional theory calculation showing the combined plot of the density of states and energy bandgap for monolayer $ReSe_2$ with an energy value of 1.26 eV.

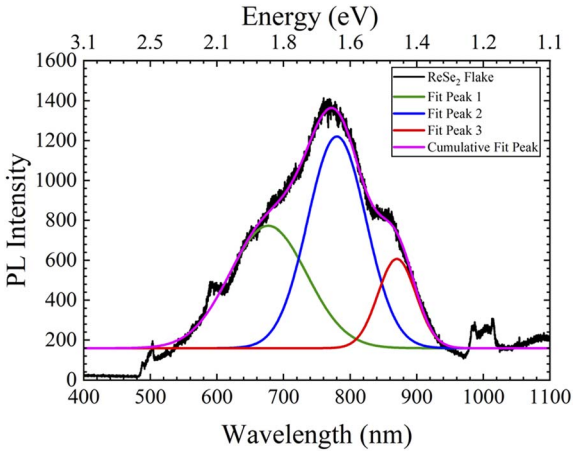


Fig. 10 The Guassian fit of room temperature PL measurement of CVD grown $ReSe_2$ flakes. The black color represents the experimental curve while the other colors green, blue, and red correspond to Guassian curves for the excitonic peaks. The peak values for the fitted curves are 670 nm (1.85 eV), 770 nm (1.61 eV) and 860 nm (1.44 eV).

Table 4 Summary of the energy bandgap for PL gaussian fits, DFT-calculated bandgap, and experimental absorption for $ReSe_2$. The peaks labeled 1,2, and 3 are obtained from the fit in Fig. 10 $ReSe_2$

| (eV) | PL (eV) | Absorption (Expt.) (eV) | DFT-bandgap (eV) |
|---|---|---|---|
| $ReSe_2$ (bulk) | | | 0.88 |
| $ReSe_2$ (monolayer) | | | 1.26 |
| Thick flakes | | 1.32 | |
| Thin flakes | | 1.40 | |
| Fit peak 3 | 1.44 | | |
| Fit peak 2 | 1.60 | | |
| Fit peak 1 | 1.85 | | |

three main peaks. For clarity purposes, the main fitted curve is split into three Gaussian curves (green, blue, and red) to accurately extract the peak positions of the shoulders in the experimental spectrum. One possible explanation of the presence of three peaks is the variation of the flake thickness as the laser spot on the flake covers a macroscopic region size of the flake (one millimeter spot size). The variation of the flake thickness is evident in the AFM profiles shown in Fig. 2. On the other hand, these three peaks represent excitonic transitions within the flake under the assumption that the electrons were undergoing transitions from the valence band to different minima in the conduction band. This is supported by the theoretical results shown in Fig. 8(a) where there are a few indirect conduction band minima. These excitonic transitions correspond to the band gap energies. The experimentally reported absorbance results for the position of the excitonic peaks shown in Fig. 8 are found to be higher than those predicted by DFT calculations. This can be attributed to the approximation method associated with DFT, which leads to bandgap underestimation. However, the observed high energy excitonic value of 1.85 eV (green curve) from Fig. 9 is consistent with the first-principles GW–Bethe–Salpeter equation prediction for $ReSe_2$ by Zhong *et al.*,[55] which is around 2.09 eV for suspended monolayer $ReSe_2$. The latter band gap value is higher than the experimental results due to depressed screening and reduced dimension, thereby enhancing quantum confinement.[17,56–58] A comparison of the band gap energies of $ReSe_2$ is shown in Table 4 where the PL, absorbance, and DFT results are presented.

## 4. Conclusion

Highly crystalline anisotropic layered $ReSe_2$ flakes with hexagonal structures were successfully grown *via* CVD. The Raman scattering spectrum reveals the presence of 18 phonon modes in the range of 100–300 $cm^{-1}$, which agrees with the computational predictions, indicating accurate phonon dispersion in the material. Density Functional Theory (DFT) calculations predicted an indirect bandgap of 0.88 eV for the bulk and 1.26 eV for the monolayer of $ReSe_2$. The absorption spectra of the grown $ReSe_2$ were found to be in the near-infrared region, between 885 and 942 nm, suggesting a layer-dependent optical response. The energy bandgap values obtained from photoluminescence measurement further confirm the layer dependent nature of $ReSe_2$ with an optical energy emission between 1.44 and 1.85 eV, this implies that its application ranges from visible to near infrared region-based optoelectronics devices. Scanning electron microscopy and energy-dispersive X-ray spectroscopy confirm the quality and morphology of the material with the profile height between 5 and 50 nm, as measured by AFM.

## Author contributions

Juwon Onasanya (J.O.): writing – original draft, software, methodology, investigation, data curation. Mourad Benamara: validation, resources, formal analysis, data curation. Kanagaraj Moorthi: validation, resources, formal analysis, data curation. Bothina Hamad (B.H.): validation, supervision, software, methodology, funding acquisition, conceptualization. H. O. H. Churchill: validation, project administration, funding acquisition, conceptualization. M. O. Manasreh: validation, supervision, project administration, funding acquisition, conceptualization.

## Conflicts of interest

The authors declare that they have no known competing financial interests or personal relationships that could have appeared to influence the work reported in this paper.

## Data availability

Data will be made available on reasonable request.

## Acknowledgements

B. H. acknowledges the support of the MonArk Quantum Foundry that is funded by the National Science Foundation Q-AMASE-i program under NSF Award No. DMR-1906383. In

addition, B. H. declares that this material is based on work supported by the National Science Foundation under Award No. DGE-2244274. J. O. declares that this material is based on research sponsored by AFRL under agreement number FA8750-24-1-1019. The U.S. Government is authorized to reproduce and distribute reprints for Governmental purposes notwithstanding any copyright notation thereon. The authors would like to thank Arkansas High Performance Computing Center (AHPCC), University of Arkansas, for the computing resources.

## References

1 A. She, Y. Zhao, J. Ni and Z. Dai, The influence of lattice anharmonicity on the thermal transport properties of two-dimensional MgF2, *J. Phys. D: Appl. Phys.*, 2024, **58**, 045305, DOI: 10.1088/1361-6463/ad8d4e.

2 J. Fang, Z. Zhou, M. Xiao, Z. Lou, Z. Wei and G. Shen, Recent advances in low-dimensional semiconductor nanomaterials and their applications in high-performance photodetectors, *InfoMat*, 2019, **2**, 291–317, DOI: 10.1002/inf2.12067.

3 K. S. Thygesen, Calculating excitons, plasmons, and quasiparticles in 2D materials and van der Waals heterostructures, *2D Mater.*, 2017, **4**, 022004, DOI: 10.1088/2053-1583/aa6432.

4 L. Du, T. Hasan, A. Castellanos-Gomez, G.-B. Liu, Y. Yao, C. N. Lau and Z. Sun, Engineering symmetry breaking in 2D layered materials, *Nat. Rev. Phys.*, 2021, **3**, 193–206, DOI: 10.1038/s42254-020-00276-0.

5 F. B. Sousa, R. Nadas, R. Martins, A. P. M. Barboza, J. S. Soares, B. R. A. Neves, I. Silvestre, A. Jorio and L. M. Malard, Disentangling doping and strain effects at defects of grown MoS2 monolayers with nano-optical spectroscopy, *Nanoscale*, 2024, **16**, 12923–12933, DOI: 10.1039/d4nr00837e.

6 S. Wang, N. T. Hung and M. Sun, Two-Dimensional Materials: From Synthesis to Applications, *Molecules*, 2025, **30**, 741, DOI: 10.3390/molecules30030741.

7 W. Xu, P. Guo, X. Li, Z. Hui, Y. Wang, Z. Shi and Y. Shu, Sheet-structured bismuthene for near-infrared dual-wavelength harmonic mode-locking, *Nanotechnology*, 2020, **31**, 225209, DOI: 10.1088/1361-6528/ab7674.

8 S.-Y. Yue, T. Xu and B. Liao, Ultralow thermal conductivity in a two-dimensional material due to surface-enhanced resonant bonding, *Mater. Today Phys.*, 2018, **7**, 89–95, DOI: 10.1016/j.mtphys.2018.11.005.

9 N. Peimyoo, H.-Y. Wu, J. Escolar, A. De Sanctis, G. Prando, F. Vollmer, F. Withers, A. C. Riis-Jensen, M. F. Craciun, K. S. Thygesen and S. Russo, Engineering Dielectric Screening for Potential-well Arrays of Excitons in 2D Materials, *ACS Appl. Mater. Interfaces*, 2020, **12**, 55134–55140, DOI: 10.1021/acsami.0c14696.

10 D. B. Straus and C. R. Kagan, Electrons, Excitons, and Phonons in Two-Dimensional Hybrid Perovskites: Connecting Structural, Optical, and Electronic Properties, *J. Phys. Chem. Lett.*, 2018, **9**, 1434–1447, DOI: 10.1021/acs.jpclett.8b00201.

11 X. Wang, T. Garcia, S. Monaco, B. Schatschneider and N. Marom, Effect of crystal packing on the excitonic properties of rubrene polymorphs, *CrystEngComm*, 2016, **18**, 7353–7362, DOI: 10.1039/c6ce00873a.

12 Y. Yang, S.-C. Liu, W. Yang, Z. Li, Y. Wang, X. Wang, S. Zhang, Y. Zhang, M. Long, G. Zhang, D.-J. Xue, J.-S. Hu and L.-J. Wan, Air-Stable In-Plane Anisotropic GeSe2 for Highly Polarization-Sensitive Photodetection in Short Wave Region, *J. Am. Chem. Soc.*, 2018, **140**, 4150–4156, DOI: 10.1021/jacs.8b01234.

13 X. Ling, H. Wang, S. Huang, F. Xia and M. S. Dresselhaus, The renaissance of black phosphorus, *Proc. Natl. Acad. Sci. U. S. A.*, 2015, **112**, 4523–4530, DOI: 10.1073/pnas.1416581112.

14 S. Puebla, R. D'Agosta, G. Sanchez-Santolino, R. Frisenda, C. Munuera and A. Castellanos-Gomez, In-plane anisotropic optical and mechanical properties of two-dimensional MoO3, *npj 2D Mater. Appl.*, 2021, **5**, 1–7, DOI: 10.1038/s41699-021-00220-5.

15 B. Aslan, D. A. Chenet, A. M. van der Zande, J. C. Hone and T. F. Heinz, Linearly Polarized Excitons in Single- and Few-Layer ReS2 Crystals, *ACS Photonics*, 2015, **3**, 96–101, DOI: 10.1021/acsphotonics.5b00486.

16 Y. Xiong, H. Chen, D. W. Zhang and P. Zhou, Electronic and Optoelectronic Applications Based on ReS2, *Phys. Status Solidi RRL*, 2019, **13**, 1800658, DOI: 10.1002/pssr.201800658.

17 V. Tran, R. Soklaski, Y. Liang and L. Yang, Layer-controlled band gap and anisotropic excitons in few-layer black phosphorus, *Phys. Rev. B: Condens. Matter Mater. Phys.*, 2014, **89**, 235319, DOI: 10.1103/physrevb.89.235319.

18 W. Dickerson, V. Tayari, I. Fakih, A. Korinek, M. Caporali, M. Serrano-Ruiz, M. Peruzzini, S. Heun, G. A. Botton and T. Szkopek, Phosphorus oxide gate dielectric for black phosphorus field effect transistors, *Appl. Phys. Lett.*, 2018, **112**, 173101, DOI: 10.1063/1.5011424.

19 N. Wang, N. Mao, Z. Wang, X. Yang, X. Zhou, H. Liu, S. Qiao, X. Lei, J. Wang, H. Xu, X. Ling, Q. Zhang, Q. Feng and J. Kong, Electrochemical Delamination of Ultralarge Few-Layer Black Phosphorus with a Hydrogen-Free Intercalation Mechanism, *Adv. Mater.*, 2020, **33**, 2005815, DOI: 10.1002/adma.202005815.

20 D. A. Chenet, B. Aslan, P. Y. Huang, C. Fan, A. M. van der Zande, T. F. Heinz and J. C. Hone, In-Plane Anisotropy in Mono- and Few-Layer ReS2 Probed by Raman Spectroscopy and Scanning Transmission Electron Microscopy, *Nano Lett.*, 2015, **15**, 5667–5672, DOI: 10.1021/acs.nanolett.5b00910.

21 H.-J. Lamfers, A. Meetsma, G. A. Wiegers and J. L. de Boer, The crystal structure of some rhenium and technetium dichalcogenides, *J. Alloys Compd.*, 1996, **241**, 34–39, DOI: 10.1016/0925-8388(96)02313-4.

22 D. Wolverson, S. Crampin, A. S. Kazemi, A. Ilie and S. J. Bending, Raman Spectra of Monolayer, Few-Layer, and Bulk ReSe2: An Anisotropic Layered Semiconductor, *ACS Nano*, 2014, **8**, 11154–11164, DOI: 10.1021/nn5053926.

23 K. Kadiwala, L. Dipane, E. Dipans, A. Bundulis, M. Zubkins, A. Ogurcovs, J. Gabrusenoks, D. Bocharov, E. Butanovs and

 

B. Polyakov, Synthesis and Investigation of ReSe2 Thin Films Obtained from Magnetron Sputtered Re and ReOx, *Crystals*, 2024, **14**, 690, DOI: 10.3390/cryst14080690.

24 S. Yang, S. Tongay, Y. Li, Q. Yue, J.-B. Xia, S.-S. Li, J. Li and S.-H. Wei, Layer-dependent electrical and optoelectronic responses of ReSe2 nanosheet transistors, *Nanoscale*, 2014, **6**, 7226, DOI: 10.1039/c4nr01741b.

25 Y. Rho, J. Pei, L. Wang, Z. Su, M. Eliceiri and C. P. Grigoropoulos, Site-Selective Atomic Layer Precision Thinning of MoS2 via Laser-Assisted Anisotropic Chemical Etching, *ACS Appl. Mater. Interfaces*, 2019, **11**, 39385–39393, DOI: 10.1021/acsami.9b14306.

26 L. Loh, Z. Zhang, M. Bosman and G. Eda, Substitutional doping in 2D transition metal ichalcogenides, *Nano Res.*, 2020, **14**, 1668–1681, DOI: 10.1007/s12274-020-3013-4.

27 J. Peng, Z.-j. Chen, B. Ding and H.-M. Cheng, Recent Advances for the Synthesis and Applications of 2-Dimensional Ternary Layered Materials, *Research*, 2023, **6**, 1–25, DOI: 10.34133/research.0040.

28 Y. Zhang, Y. Yao, M. G. Sendeku, L. Yin, X. Zhan, F. Wang, Z. Wang and J. He, Recent Progress in CVD Growth of 2D Transition Metal Dichalcogenides and Related Heterostructures, *Adv. Mater.*, 2019, **31**, 1901694, DOI: 10.1002/adma.201901694.

29 J. Li, Q. Zhou, C. Yuan, P. Cheng, X. Hu, W. Huang, X. Gao, X. Wang, M. Jin, R. Nötzel, G. Zhou, Z. Zhang and J. Liu, Direct growth of vertically aligned ReSe2 nanosheets on conductive electrode for electro-catalytic hydrogen production, *J. Colloid Interface Sci.*, 2019, **553**, 699–704, DOI: 10.1016/j.jcis.2019.06.073.

30 G. Kresse and J. Hafner, Ab initio molecular dynamics for liquid metals, *Phys. Rev. B*, 1993, **47**, 58–561, DOI: 10.1103/physrevb.47.558.

31 G. Kresse and J. Furthmüller, Efficient iterative schemes forab initiototal-energy calculations using a plane-wave basis set, *Phys. Rev. B*, 1996, **54**, 11169–11186, DOI: 10.1103/physrevb.54.11169.

32 J. P. Perdew, K. Burke and M. Ernzerhof, Generalized Gradient Approximation Made Simple, *Phys. Rev. Lett.*, 1996, **77**, 3865–3868, DOI: 10.1103/physrevlett.77.3865.

33 J. Klimeš, D. R. Bowler and A. Michaelides, Van der Waals density functionals applied to solids, *Phys. Rev. B:Condens. Matter Mater. Phys.*, 2011, **83**, 195131, DOI: 10.1103/physrevb.83.195131.

34 S. Baroni, S. de Gironcoli, A. Dal Corso and P. Giannozzi, Phonons and related crystal properties from density-functional perturbation theory, *Rev. Mod. Phys.*, 2001, **73**, 515–562, DOI: 10.1103/revmodphys.73.515.

35 M. Hafeez, L. Gan, H. Li, Y. Ma and T. Zhai, Chemical Vapor Deposition Synthesis of Ultrathin Hexagonal ReSe2 Flakes for Anisotropic Raman Property and Optoelectronic Application, *Adv. Mater.*, 2016, **28**, 8296–8301, DOI: 10.1002/adma.201601977.

36 K. Keyshar, Y. Gong, G. Ye, G. Brunetto, W. Zhou, D. P. Cole, K. Hackenberg, Y. He, L. Machado, M. Kabbani, A. H. C. Hart, B. Li, D. S. Galvao, A. George, R. Vajtai, C. S. Tiwary and P. M. Ajayan, Chemical Vapor Deposition of Monolayer Rhenium Disulfide (ReS2), *Adv. Mater.*, 2015, **27**, 4640–4648, DOI: 10.1002/adma.201501795.

37 P. Sutter and E. Sutter, Unconventional van der Waals heterostructures beyond stacking, *iScience*, 2021, **24**, 103050, DOI: 10.1016/j.isci.2021.103050.

38 B. Jariwala, D. Voiry, A. Jindal, B. A. Chalke, R. Bapat, A. Thamizhavel, M. Chhowalla, M. Deshmukh and A. Bhattacharya, Synthesis and Characterization of ReS2 and ReSe2 Layered Chalcogenide Single Crystals, *Chem. Mater.*, 2016, **28**, 3352–3359, DOI: 10.1021/acs.chemmater.6b00364.

39 V. O. Yukhymchuk, L. M. Kulikov, M. Y. Valakh, A. P. Litvinchuk, M. A. Skoryk, N. V. Mazur, V. S. Yefanov, O. Selyshchev, V. M. Dzhagan and D. R. T. Zahn, Structure and vibrational spectra of ReSe2 nanoplates, *J. Raman Spectrosc.*, 2020, **51**, 1305–1314, DOI: 10.1002/jrs.5898.

40 E. Lorchat, G. Froehlicher and S. Berciaud, Splitting of Interlayer Shear Modes and Photon Energy Dependent Anisotropic Raman Response in N-Layer ReSe2 and ReS2, *ACS Nano*, 2016, **10**, 2752–2760, DOI: 10.1021/acsnano.5b07844.

41 K. Friemelt, M.-C. Lux-Steiner and E. Bucher, Optical properties of the layered transition-metal-dichalcogenide ReS2: Anisotropy in the van der Waals plane, *J. Appl. Phys.*, 1993, **74**, 5266–5268, DOI: 10.1063/1.354268.

42 S. Y. Park, H. Rho, J. D. Song, S. Lee, G. Kim and C. H. Lee, Spatially-resolved and polarized Raman scattering from a single Si nanowire, *J. Raman Spectrosc.*, 2015, **46**, 524–530, DOI: 10.1002/jrs.4689.

43 R. P. N. Tripathi, X. Yang and J. Gao, -dependent optical responses in natural 2D layered mineral teallite, *Sci. Rep.*, 2021, **11**, 21895, DOI: 10.1038/s41598-021-01511-z.

44 Z. Shu, Q. Peng, P. Huang, Z. Xu, A. A. Suleiman, X. Zhang, X. Bai, X. Zhou and T. Zhai, of Ultrathin Ternary Teallite (PbSnS2) Flakes for Highly Anisotropic Optoelectronics, *Matter*, 2020, **2**, 977–987, DOI: 10.1016/j.matt.2020.01.013.

45 G. Nam, S. Park, K. Heo, J. Bong, D. Lee, H. Kim, K. M. Ponnusamy, H. Bae, H. G. Park, J.-H. Lee and H.-S. Jang, An in-depth study of the synthesis of ReSe2 for anisotropic Raman characteristics, *J. Phys.: Mater.*, 2024, **7**, 045005, DOI: 10.1088/2515-7639/ad8033.

46 F. Cui, X. Li, Q. Feng, J. Yin, L. Zhou, D. Liu, K. Liu, X. He, X. Liang, S. Liu, Z. Lei, Z. Liu, H. Peng, J. Zhang, J. Kong and H. Xu, Epitaxial growth of large-area and highly crystalline anisotropic ReSe2 atomic layer, *Nano Res.*, 2017, **10**, 2732–2742, DOI: 10.1007/s12274-017-1477-7.

47 Y.-C. Jian, D.-Y. Lin, J.-S. Wu and Y.-S. Huang, Optical and Electrical Properties of Au- and Ag-Doped ReSe2, *Jpn. J. Appl. Phys.*, 2013, **52**, 04CH06, DOI: 10.7567/jjap.52.04ch06.

48 Y. S. Huang, C. H. Ho, P. C. Liao and K. K. Tiong, Temperature dependent study of the band edge excitons of ReS2 and ReSe2, *J. Alloys Compd.*, 1997, **262–263**, 92–96, DOI: 10.1016/s0925-8388(97)00335-6.

49 R. Dutta, A. Bala, A. Sen, M. R. Spinazze, H. Park, W. Choi, Y. Yoon and S. Kim, Optical Enhancement of Indirect Bandgap 2D Transition Metal Dichalcogenides for Multi-

Functional Optoelectronic Sensors, *Adv. Mater.*, 2023, **35**, DOI: 10.1002/adma.202303272.

50 H. Zhao, J. Wu, H. Zhong, Q. Guo, X. Wang, F. Xia, L. Yang, P. Tan and H. Wang, Interlayer interactions in anisotropic atomically thin rhenium diselenide, *Nano Res.*, 2015, **8**, 3651–3661, DOI: 10.1007/s12274-015-0865-0.

51 E. Zhang, P. Wang, Z. Li, H. Wang, C. Song, C. Huang, Z.-G. Chen, L. Yang, K. Zhang, S. Lu, W. Wang, S. Liu, H. Fang, X. Zhou, H. Yan, J. Zou, X. Wan, P. Zhou, W. Hu and F. Xiu, Tunable Ambipolar Polarization-Sensitive Photodetectors Based on High-Anisotropy ReSe2 Nanosheets, *ACS Nano*, 2016, **10**, 8067–8077, DOI: 10.1021/acsnano.6b04165.

52 S. Ojo, J. Onasanya, M. Benamara, B. Hamad and M. O. Manasreh, Optical spectroscopy of excitons in ReS2 monolayers grown by chemical vapor deposition, *Opt. Mater.*, 2025, **160**, 116729, DOI: 10.1016/j.optmat.2025.116729.

53 J.-Q. Zong, W.-X. Ji, P. Li and P.-J. Wang, The biaxial strain induced properties of ReX2 and ReXS (X = S, Se, Te) monolayers, *Mater. Res. Express*, 2020, **7**, 055018, DOI: 10.1088/2053-1591/ab7218.

54 A. Arora, J. Noky, M. Drüppel, B. Jariwala, T. Deilmann, R. Schneider, R. Schmidt, O. Del Pozo-Zamudio, T. Stiehm, A. Bhattacharya, P. Krüger, S. Michaelis de Vasconcellos, M. Rohlfing and R. Bratschitsch, Highly Anisotropic in-Plane Excitons in Atomically Thin and Bulklike 1T′-ReSe2, *Nano Lett.*, 2017, **17**, 3202–3207, DOI: 10.1021/acs.nanolett.7b00765.

55 H.-X. Zhong, S. Gao, J.-J. Shi and L. Yang, Quasiparticle band gaps, excitonic effects, and anisotropic optical properties of the monolayer distorted 1Tdiamond-chain structures $ReS_2$ and $ReSe_2$, *Phys. Rev. B: Condens. Matter Mater. Phys.*, 2015, **92**, 115438, DOI: 10.1103/physrevb.92.115438.

56 D. Y. Qiu, F. H. da Jornada and S. G. Louie, Optical Spectrum of $MoS_2$: Many-Body Effects and Diversity of Exciton StatesMany-Body Effects and Diversity of Exciton States, *Phys. Rev. Lett.*, 2013, **111**, 216805, DOI: 10.1103/physrevlett.111.216805.

57 C. D. Spataru, S. Ismail-Beigi, L. X. Benedict and S. G. Louie, Excitonic Effects and Optical Spectra of Single-Walled Carbon Nanotubes, *Phys. Rev. Lett.*, 2004, **92**, 077402, DOI: 10.1103/physrevlett.92.077402.

58 A. Ramasubramaniam, Large excitonic effects in monolayers of molybdenum and tungsten dichalcogenides, *Phys. Rev. B: Condens. Matter Mater. Phys.*, 2012, **86**, 115409, DOI: 10.1103/physrevb.86.115409.